2005 American Control Conference
June 8-10, 2005. Portland, OR, USA

Nanopositioning for Probe Storage

A. Sebastian, A. Pantazi, G. Cherubini, E. Eleftheriou, M. A. Lantz and H. Pozidis
IBM Zürich Research Laboratory
CH-8803 Rüschlikon, Switzerland

Abstract— **Scanning-probe data-storage devices are currently being explored as alternatives to conventional data storage. Ultra-high density, small form factor, and low cost are thought to be the primary advantages of probe storage. The ultra-high areal density makes nanopositioning a significant challenge in probe storage. In this paper we discuss the control of a MEMS scanner used in a probe storage device which uses thermo-mechanical means to store and retrieve information on thin polymer films. The MEMS scanner has X-Y motion capabilities with a travel range of approx 120 μm. Thermal position sensors are used to provide positioning information. This paper describes the dynamics of the micro-scanner, the primary control challenges, and the way they are addressed.**

I. Introduction

In the past decade, there has been a tremendous increase in the storage density of conventional data-storage technologies such as magnetic recording and solid-state flash memory. However, the areal densities that current magnetic recording technologies can achieve will eventually reach a limit imposed by the super-paramagnetic effect, which for longitudinal recording is conjectured to be on the order of 250 Gbit/in^2. In the case of semiconductor flash memory, the challenge is of lithographic nature, in that it is becoming increasingly difficult to define and fabricate sub-90-nm FET gates in a cost-effective manner.

The capability of scanning probes not only to image but also to modify samples at the nano-scale has motivated efforts to create data-storage devices based on scanning-probe techniques that store data at much higher areal densities than can be achieved conventionally [1]. However, the main challenge in probe storage is speed. To date the maximum readback data rates that have been demonstrated by probe storage devices range from 0.1 to 1 Mbit/s for a single probe. Thus, the speed must be increased by several orders of magnitude for them to become comparable to conventional storage devices. One solution to achieve such a substantial increase in the data rate is to use a MEMS-based array of probes operating in parallel, where each probe performs write/read/erase operations on an individual storage field. In [2] one such scheme is described with cantilevers acting as the probes where each cantilever operates on an individual storage field with an area on the order of 100 μm $\times$ 100 μm. A thermo-mechanical scheme is employed to write/read/erase data on the storage medium which is a thin polymer film. This thermo-mechanical probe-based data-storage approach combines ultra-high density, small form factor, and high data rates by means of parallel operation of a large number of probes.

Digital information is stored by making indentations on the thin polymer film using the tips of the cantilevers, which are a few nanometers in diameter. Thermo-mechanical writing is achieved by applying a force through the cantilever/tip to the polymer layer and simultaneously softening the polymer layer by local heating. To read the written information, the cantilever originally used for writing is given the additional function of a thermal readback sensor by exploiting its temperature-dependent resistance. The shape of a typical indentation resembles an almost conical structure with a diameter of approx. 15 to 30 nm. This indentation shape results in an error-rate performance that rapidly deteriorates as the probe-tip distance from the center of the indentation increases. In particular, the error rate was found to increase by one order of magnitude at a distance of 4 nm from the indentation center. This deterioration of off-track performance is characteristic of probe storage with nanometer-sharp probe tips used as both write and read transducers. Hence nanopositioning plays a central role in probe storage. One can think of the lithographic challenges, that is of having to make ultra small memory cells such as in flash memory, being translated to the more tractable challenges in positioning accuracy.

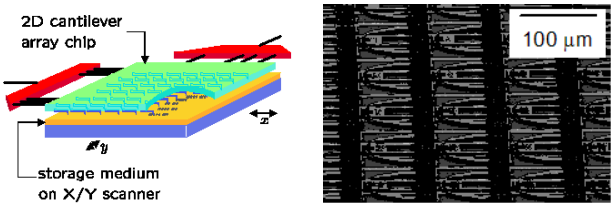

(a) (b)

Fig. 1. (a) Schematic of the storage device. (b) Scanning electron microscope image showing a section of the chip with the array of cantilevers.

A large 2D array consisting of up to 4096 cantilevers with integrated tips, sensors and actuators has been fabricated using silicon micromachining techniques. Fig. 1(a) shows a schematic of the storage device and Fig. 1(b) shows a section of the fabricated chip. To position the large array of probe tips over the storage medium, a MEMS-based X-Y scanner is employed [3].

The scanner has X-Y displacement capabilities of about 120 μm. The mechanical components of the scanner are fabricated from a 400-μm-thick silicon wafer using a deep-trench-etching process. This scanner chip is then mounted on a silicon base plate that acts as the mechanical ground of the system. The base plate has been designed to provide a clearance of about 20 μm between its top surface and the bottom surface of the moving parts of the scanner. The scan table, which carries the polymer storage medium, can be displaced in the X and Y directions in the plane of the

0-7803-9098-9/05/$25.00 ©2005 AACC

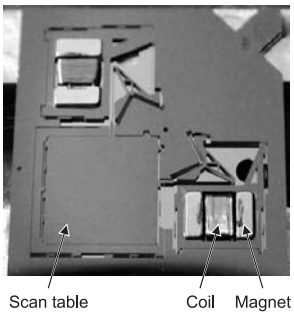

Fig. 2. Picture of the microscanner.

silicon wafer. Two voice coil actuators are used to actuate the scanner in the X and Y directions (see Fig. 2).

Two pairs of thermal position sensors are used to provide X-Y position information of the scanner. The sensors consist of thermally isolated, resistive strip heaters made from moderately doped silicon and are positioned directly above the scan table. Displacement of the scan table translates into a change in the temperature of these heaters and thus a change in their electrical resistance. The noise introduced by these sensors plays a significant role in the positioning accuracy and is denoted by n_{xt} and n_{yt}, respectively. The sensor signals are sampled using 14-bit analog-to-digital converters (ADCs), which introduce a second source of noise due to quantization effects.

II. Modeling and Identification

Assuming that there is no coupling between the horizontal (X direction) and vertical (Y direction), the scanner can be modeled by two linear systems. The transfer function P_{xx} maps the coil current (u_x in mA) to the output displacement x (in μm) and the transfer function P_{yy} maps u_y to y (see Fig. 3).

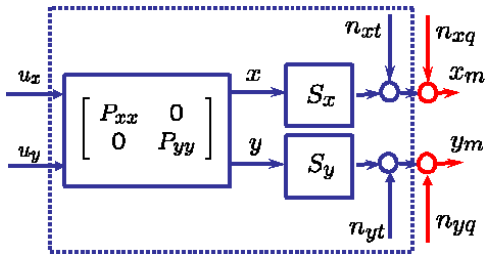

Fig. 3. The scanner is modeled by two linear systems P_{xx} and P_{yy}. The thermal sensors are modeled as constant gains S_x and S_y with additive noise n_{xt} and n_{yt}, respectively.

To identify P_{xx} and P_{yy}, the frequency responses of the scanner in the X and Y directions are obtained using the thermal sensors over the range from 0 to 3.5 kHz. The thermal sensors introduce no additional dynamics over this range of frequencies and can be assumed to be constant. The experimental frequency response of the Y axis is shown in Fig. 4. As can be seen, the dynamics is dominated by the first mode and can be accurately captured by a simple

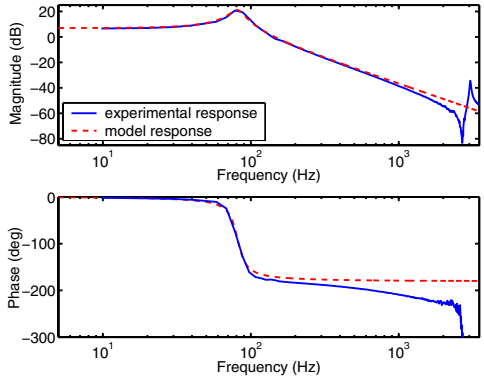

Fig. 4. Measured frequency response of the Y axis compared with the frequency response of the model P_{yy}.

second-order model. The frequency response of P_{xx} has a resonant frequency of 93.2 Hz, and the frequency response of P_{yy} has a resonant frequency of 81.9 Hz. The quality factors are in both cases approximately 8.

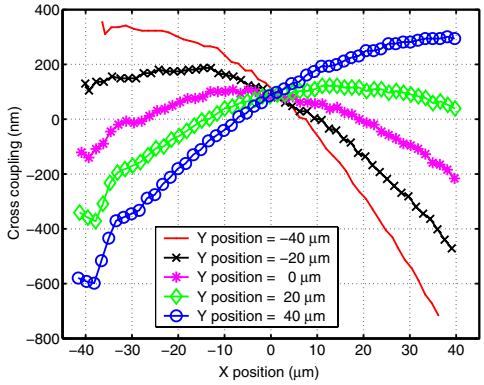

Fig. 5. Cross-coupling of the X motion onto the Y axis for different Y positions.

There is some cross-coupling between the X and Y axes as shown in Fig. 5. This cross-coupling is a function of the position, x and y, and is nonlinear. The approach employed is not to model this explicitly but to treat the cross-coupling as a disturbance signal that needs to be rejected by the controller.

III. Controller Design

A. Control challenges

The thermal position sensors and low-resolution ADCs are advantageous in terms of costs. However, the intrinsic noise from these sensors and the limited resolution of the ADCs pose a significant challenge to the achievable close loop positioning resolution. Speeds of a few nanometers per microsecond are required to achieve data rates on the order of 50 kbit/s Hence bandwidth is also of great significance in probe storage besides positioning accuracy. Moreover, disturbance rejection is of great importance to deal with external disturbances. The controller should also

be robust against friction and other forces due to multiple probes interacting with the scanner while reading and writing. In addition, as the feedback controller does not address cross-coupling between the axes explicitly, good disturbance rejection capabilities are needed to address the cross-coupling between the axes. Finally, robustness against model variations is another key requirement for the feedback regulators because the scanner dynamics may change because of changes in the ambient environment as well as aging effects.

B. Control architecture

The controller for the X-Y scanner consists of a linear quadratic Gaussian (LQG) regulator, a tracking controller and a feed-forward component. This is depicted in Fig. 6, where the block diagram of the feedback loop for the Y axis is shown. The transfer function $\widehat{P_{yy}}$ denotes the observer for P_{yy}. A pure integrator is used as tracking controller, and K_{ff_y} denotes the feed-forward component of the controller. A similar loop exists for the X axis. A detailed analysis of this feedback loop is provided in terms of its tracking performance, disturbance rejection, resolution, and robustness. Moreover, a frequency domain analysis of the control architecture enables a direct comparison with modern frequency domain designs, such as the $\mathscr{H}_\infty$ and Glover-McFarlane $\mathscr{H}_\infty$ loop-shaping designs.

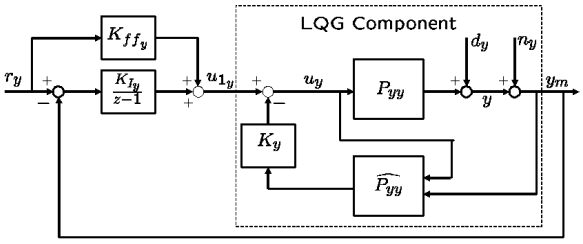

Fig. 6. Block diagram of the control architecture in the Y direction consisting of an LQG regulator, a tracking controller (an integrator) and a feed-forward component.

C. Bandwidth, resolution, and disturbance rejection

It is essential to have a quantitative measure of the performance characteristics, i.e. bandwidth, resolution, and disturbance rejection. The transfer function relating the reference with the error signal is a good measure of the tracking performance or the bandwidth. Similarly, the transfer function relating the disturbance signal with the output gives a quantitative measure of the disturbance-rejection capabilities of the controller. The transfer function relating the noise signal with the output measures the impact of measurement noise on the output and hence is a good measure of resolution.

To analyze the bandwidth, resolution and disturbance rejection of the feedback loop in Fig. 6, it is advantageous to first analyze the LQG component. The transfer functions from input u_{1_y}, from disturbance signal d_y, and from noise signal n_y, to the output y are evaluated for this block.

Let the discretized version of the dynamics of the scanner in the Y direction in the absence of disturbance be described by

$$\begin{aligned} \mathbf{x}(k+1) &= F_y\mathbf{x}(k)+G_y u_y(k) && (1)\\ y(k) &= H_y\mathbf{x}(k), && (2)\end{aligned}$$

and the dynamics of the Kalman filter be given by

$$\begin{aligned} \hat{\mathbf{x}}(k+1) &= (F_y-L_yH_y)\hat{\mathbf{x}}(k)+G_y u_y(k)+L_y y_m(k) && (3)\\ \bar{\mathbf{x}}(k) &= (I-M_yH_y)\hat{\mathbf{x}}(k)+M_y y_m(k), && (4)\end{aligned}$$

where $\hat{\mathbf{x}}$ is $\hat{\mathbf{x}}(k/k-1)$ and $\bar{\mathbf{x}}$ is $\hat{\mathbf{x}}(k/k)$. Moreover, L_y and M_y are the observer gains, and $L_y = F_yM_y$.

First the transfer function relating the input to the loop u_{1_y} with the output y is evaluated. Let this transfer function be denoted by $\overline{T_{ref}}$. Let also $A_{cl} = \begin{bmatrix} F_y-G_yK_yM_yH_y & -G_yK_y(I-M_yH_y) \\ LyHy-G_yK_yM_yH_y & F_y-L_yH_y-G_yK_y(I-M_yH_y)\end{bmatrix}$, then

$$\overline{T_{ref}} \stackrel{s}{=} \left[\begin{array}{c|c} A_{cl} & \begin{pmatrix} G_y \\ G_y\end{pmatrix} \\ \hline \begin{pmatrix} H_y & 0\end{pmatrix} & 0\end{array}\right]. \quad (5)$$

Similarly, the transfer functions relating the disturbance signal d_y with the output y, denoted by $\overline{S_{dis}}$, and the transfer function relating the noise signal n_y with the output y, denoted by $\overline{T_{noise}}$ are evaluated. $\overline{S_{dis}}$ is described by

$$\overline{S_{dis}} \stackrel{s}{=} \left[\begin{array}{c|c} A_{cl} & \begin{pmatrix} -G_yK_yM_y \\ Ly-G_yK_yM_y\end{pmatrix} \\ \hline \begin{pmatrix} H_y & 0\end{pmatrix} & 1\end{array}\right], \quad (6)$$

and $\overline{T_{noise}}$ is described by

$$\overline{T_{noise}} \stackrel{s}{=} \left[\begin{array}{c|c} A_{cl} & \begin{pmatrix} -G_yK_yM_y \\ Ly-G_yK_yM_y\end{pmatrix} \\ \hline \begin{pmatrix} H_y & 0\end{pmatrix} & 0\end{array}\right] \quad (7)$$

The poles of these transfer functions can be shown to be equal to the eigenvalues of $(F_y - G_yK_y)$ and $(F_y - L_yH_y)$, as expected from the separation principle. Unlike a one-degree-of-freedom feedback loop, the relation between these transfer functions is not straightforward. However, $\overline{S_{dis}}$ and $\overline{T_{noise}}$ are linked in a direct way. This can be shown by analyzing the LQG component as a two-degrees-of-freedom feedback loop.

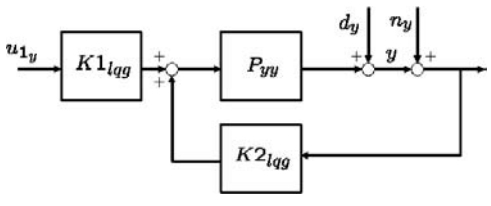

Fig. 7. Two-degrees-of-freedom configuration of the LQG component.

In the two-degrees-of-freedom framework, the LQG component appears as shown in Fig. 7, where the pre-filter $K1_{lqg}$ is given by

$$K1_{lqg} \overset{s}{=} \left[\begin{array}{c|c} F_y - L_y H_y - G_y K_y (I - M_y H_y) & G_y \\ \hline -K_y (I - M_y H_y) & 1 \end{array}\right], \quad (8)$$

and the feedback component $K2_{lqg}$ is given by

$$K2_{lqg} \overset{s}{=} \left[\begin{array}{c|c} F_y - L_y H_y - G_y K_y (I - M_y H_y) & L_y - G_y K_y M_y \\ \hline -K_y (I - M_y H_y) & -K_y M_y \end{array}\right]. \quad (9)$$

From Fig. 7 it is straightforward to obtain the three transfer functions $\overline{T_{ref}}$, $\overline{S_{dis}}$, and $\overline{T_{noise}}$, i.e., $\overline{T_{ref}} = \frac{K1_{lqg} P_{yy}}{1 - P_{yy} K2_{lqg}}$, $\overline{S_{dis}} = \frac{1}{1 - P_{yy} K2_{lqg}}$, and $\overline{T_{noise}} = \frac{P_{yy} K2_{lqg}}{1 - P_{yy} K2_{lqg}}$.

Note that $\overline{T_{noise}} = 1 - \overline{S_{dis}}$, which shows the direct link between the two transfer functions. But unlike a one-degree-of-freedom feedback loop, $\overline{T_{noise}}$ is not equal to $\overline{T_{ref}}$.

Using $\overline{T_{ref}}$, $\overline{S_{dis}}$, and $\overline{T_{noise}}$, the transfer functions which serve as measures of bandwidth, resolution, and disturbance rejection for the entire control loop in Fig. 6 are obtained. In our controller architecture we have considered an integral controller for tracking as shown in Fig. 6. Clearly such a choice is a special case of a generic tracking controller $K_{tr_y}(z)$. For the overall feedback loop, the transfer function between the reference and the output is given by T_{ref}. A better measure of the tracking performance is S_{ref}, which is the transfer function from the reference to the error signal. It can readily be shown that the transfer functions T_{ref} and S_{ref} are given by

$$T_{ref} = \frac{\overline{T_{ref}} K_{tr_y} + \overline{T_{ref}} K_{ff_y}}{1 + \overline{T_{ref}} K_{tr_y}}, \; S_{ref} = \frac{1 - \overline{T_{ref}} K_{ff_y}}{1 + \overline{T_{ref}} K_{tr_y}}. \quad (10)$$

Similarly, it can be shown that the transfer functions between the disturbance and noise to the output y, denoted by S_{dis} and T_{noise}, respectively, are given by

$$S_{dis} = \frac{\overline{S_{dis}}}{1 + \overline{T_{ref}} K_{tr_y}}, \; T_{noise} = \frac{\overline{T_{noise}} - \overline{T_{ref}} K_{tr_y}}{1 + \overline{T_{ref}} K_{tr_y}}. \quad (11)$$

IV. Experimental Results and Discussion

In this section we evaluate the performance of the implemented controller in terms of bandwidth, disturbance-rejection capabilities, and resolution.

A. Tracking performance

As mentioned above, the closed-loop transfer functions T_{ref} and S_{ref} can be used as measures of the tracking performance. In regions where the magnitude response of S_{ref} is small, the output signal tracks the reference well in both magnitude and phase. Hence to quantify the tracking performance S_{ref} is preferred to T_{ref}. The magnitude response of S_{ref} for the X and Y axes is depicted in Fig. 8. The closed-loop bandwidth in the X direction is 175 Hz, and that in the Y direction is 150 Hz. For the X axis, which is the fast scan axis, the feed-forward component is selected to be equal to the inverse of the DC gain of P_{xx} in order to achieve better tracking performance, whereas for the Y axis, the feed-forward component is selected to cancel the closed-loop pole created by the integrator to achieve better

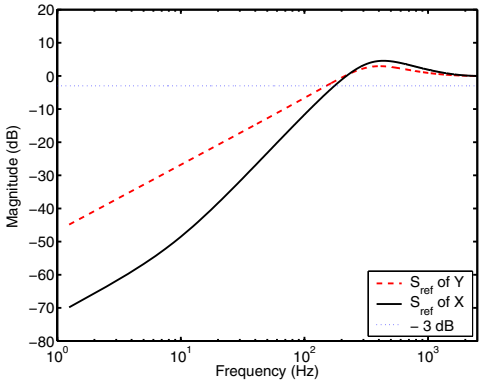

Fig. 8. Magnitude response of S_{ref} shown for both X and Y axis.

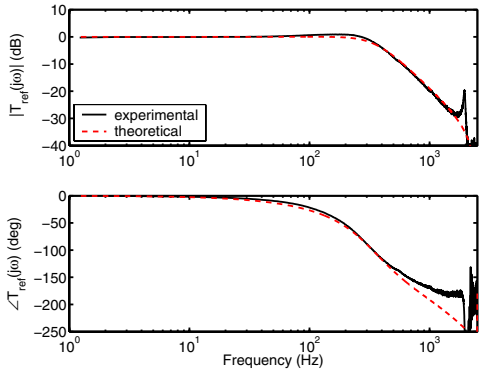

Fig. 9. Analytical and experimental frequency response of the closed-loop transfer function T_{ref} for the Y axis.

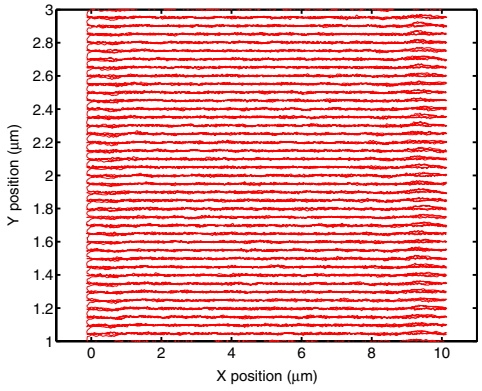

Fig. 10. Typical scan operation in the device, where the scanner follows a triangular reference signal in the X direction and steps from track to track in the Y direction.

transient response while stepping from track to track. The experimental and analytical frequency responses of T_{ref} for the Y axis are compared in Fig. 9. There is remarkable agreement between the two. The flat magnitude response indicates that the closed-loop pole introduced by the integrator is well cancelled by the feed-forward component. Fig. 10 shows a typical scan performed with the data storage device while reading or writing information. A scan is performed

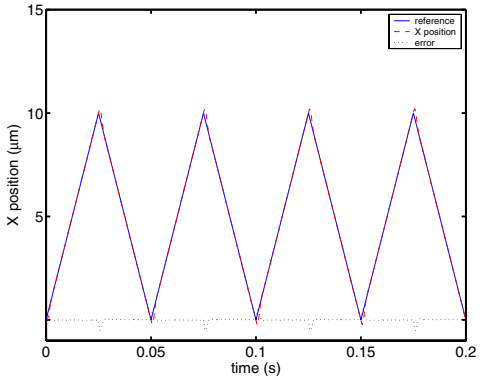

Fig. 11. Performance of the scanner in the X direction following a triangular reference signal of 20 Hz.

along the X direction, while stepping from track to track in the Y direction. In this particular scan the reference signal for the X axis is a triangular waveform with a frequency of 10 Hz. Fig. 11 depicts the motion of the X axis while scanning at 20 Hz. Except for the turnarounds, the tracking is very good.

B. Disturbance rejection

The disturbance rejection capabilities of the feedback loop are captured by the transfer function, S_{dis}. Fig. 12 shows the analytical and experimental frequency response corresponding to this transfer function. Note that S_{dis} is quite different from S_{ref}, unlike a one-degree-of-freedom control architecture where $S_{dis} = S_{ref}$. From Fig. 12 it can be seen that S_{dis} cannot adequately reject disturbances beyond approximately 125 Hz. Moreover, most of the disturbances such as physical shocks and those due to cross-coupling fall into this frequency region.

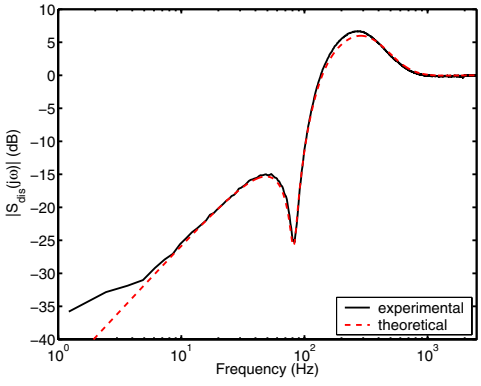

Fig. 12. Comparison of analytical frequency response with the experimentally measured response of S_{dis} for the Y axis.

C. Resolution

As mentioned earlier, positioning accuracy is of great significance for probe storage. The transfer function that measures the impact of measurement noise is T_{noise}. The experimentally obtained frequency response of T_{noise} for the X and Y axis is shown in Fig. 13. They match very well with the analytical response of T_{noise}.

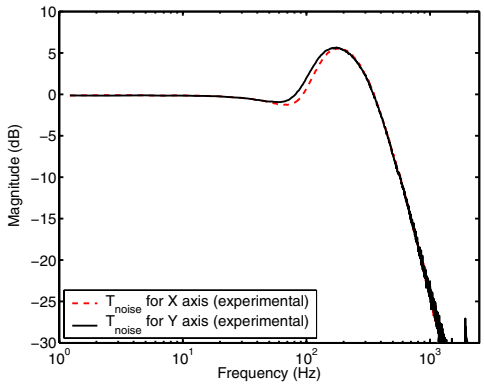

Fig. 13. Experimental frequency response of the closed-loop transfer function T_{noise} for X and Y axis.

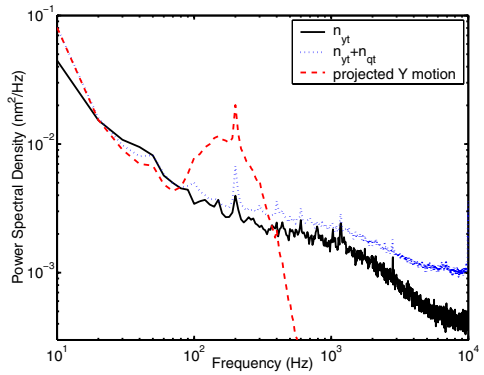

Fig. 14. Comparison of contributions of thermal sensor and data-acquisition system to the total measurement noise. By filtering this sensor noise with the closed-loop transfer function T_{noise}, the closed-loop positioning resolution is measured.

To illustrate the positioning resolution, the noise characteristics of the thermal sensor and the ADC are presented for the Y axis. The power spectral densities of these two noise sources are shown in Fig. 14. The thermal sensor noise has a standard deviation of 2.35 nm over 10 kHz bandwidth. However, this noise is quite colored with a significant low-frequency component. The quantization noise on the other hand can be assumed to be discrete white noise, and the combined sensor noise has a standard deviation of 4.1 nm over 10 kHz bandwidth. The projected motion of the scanner due to this sensor noise can be obtained by filtering the sensor noise with T_{noise}, which yields a standard deviation of 2.28 nm. Note that by implementing the controller at higher sampling frequencies, the impact of quantization noise can be further reduced. The sensor noise and quantization noise limit the capabilities of the feedback loop to provide higher bandwidth and higher disturbance-rejection capabilities. But this is an inherent trade-off in any control design, which is of even greater importance in

probe storage, where nanometer-scale positioning accuracy is desired.

Fig. 15 shows the simultaneous readback of data from four storage fields using four probes and employing the servo scheme discussed in this paper.

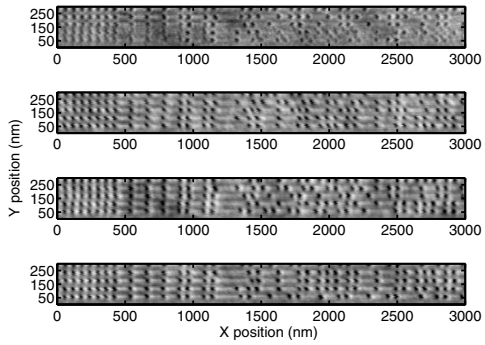

Fig. 15. Parallel reading of recorded indentations from four storage fields. The control scheme described in this paper is used for both reading and writing.

D. Robustness

Robustness is not as much an issue in the current MEMS scanner as it is in other larger nanopositioners in which flexure stages and piezo-actuators are employed. The frequency responses in the X and Y directions remain fairly constant throughout the travel range of the scanner. They also seem to remain constant as a function of time.

E. Comparison with other control architectures

Besides the control architecture described earlier, frequency domain controllers such as the nominal $\mathscr{H}_\infty$ [4] and the Glover McFarlane loop-shaping designs [5] were designed and implemented for the microscanner. The experimentally obtained closed-loop responses for one of the $\mathscr{H}_\infty$ designs are shown in Fig. 16. The bandwidth versus resolution trade-off is elegantly captured by the fact that $T_{noise} = 1 - S_{ref}$ in the one-degree-of-freedom feedback loop. Hence the desired tracking bandwidth fixes the achievable positioning resolution in the presence of noise. This is slightly different in the control architecture described earlier in which T_{noise} is not equal to $1 - S_{ref}$. However, the most significant drawback of the $\mathscr{H}_\infty$ design is the inability to enforce zero steady-state error-tracking by having controller poles at zero.

Glover McFarlane loop-shaping designs are particularly suitable for systems which have specific tracking requirements. However, the absence of pole-zero uncertainty in the MEMS scanner does not justify the use of such a controller. These controllers do not cancel the plant resonance exactly [6], which could be a drawback in scenarios where the plant resonance does not deviate significantly from the nominal value. The Glover McFarlane design, which was found to be an excellent choice for piezo-driven flexure stages [7], proved inappropriate for the current application.

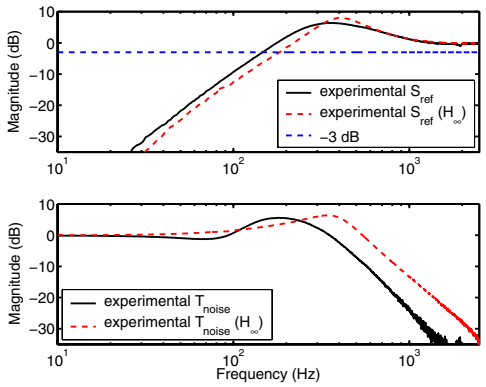

Fig. 16. Experimentally obtained frequency responses of the closed-loop transfer functions S_{ref} and T_{noise} for nominal $\mathscr{H}_\infty$ are compared with those obtained using the control architecture described in Section III

V. Conclusions

Nanopositioning is a crucial aspect of probe storage because of the ultra high areal densities the nanoscale indentation pitch. This paper describes the control design for a MEMS scanner used in a probe-storage prototype in which thermal position sensors are used to provide positioning information. The various control challenges are outlined, and the control architecture is presented along with a quantitative assessment of the performance in terms of bandwidth, resolution, and disturbance-rejection capabilities.

VI. Acknowledgements

We thank our colleagues of the Storage Technologies and Nanomechanics groups at the IBM Zurich Research Laboratory. Special thanks go to M. Despont, U. Drechsler, D. Jubin and H. Rothuizen for the design and fabrication of MEMS parts and to P. Bächtold for the design of the electronics used in this work.

References

[1] H. J. Mamin, R. P. Ried, B. D. Terris, and D. Rugar. High-density data storage based on the atomic force microscope. *Proceedings of the IEEE*, 87, 1999.

[2] E. Eleftheriou, T. Antonakopoulos, G. K. Binnig, G. Cherubini, M. Despont, A. Dholakia, U. Durig, M. A. Lantz, H. Pozidis, H. E. Rothuizen, and P. Vettiger. Millipede-a MEMS based scanning-probe data storage system. *IEEE Transactions on Magnetics*, 39(2):pp. 938–945, 2003.

[3] A. Pantazi, M. A. Lantz, G. Cherubini, H. Pozidis, and E. Eleftheriou. A servomechanism for a micro-electro-mechanical-system-based scanning-probe data storage device. *Nanotechnology*, 15:612–621, August 2004.

[4] S. Skogestad and I. Postlethwaite. *Multivariable Feedback Control, Analysis and Design*. John Wiley and Sons, 1997.

[5] K. Glover and D. McFarlane. Robust stabilization of normalized coprime factor plant descriptions with $\mathscr{H}_\infty$-bounded uncertainty. *IEEE Transactions on Automatic Control*, 34(8):821–830, August 1989.

[6] J. Sefton and K. Glover. Pole/zero cancellations in the general $\mathscr{H}_\infty$ problem with reference to a two block design. *Systems and Control Letters*, 14(4), 1990.

[7] A. Sebastian and S. Salapaka. $\mathscr{H}_\infty$ loop shaping design for nanopositioning. In *Proceedings of the American Control Conference, Denver, Colorado*, June 2003.